Progress In Electromagnetics Research, PIER 12, 303–333, 1996

MUELLER MATRICES FOR SCATTERING FROM CHIRAL COATED CURVED SURFACES

J. C. Liu and D. L. Jaggard

1. Introduction

Electromagnetic chirality describes the effect of handedness in electrodynamics. Since chirality gives rise to handedness, circularly polarized waves of different handedness have characteristic interactions with chiral media. This means that two wavenumbers are present, one of each circularly polarized mode, and a given object will appear to be one of two sizes depending upon the polarization of the illuminating wave [1,2]. For this reason, several canonical curved geometries coated with chiral layers are examined to quantify this polarization effect on angular scattering. The geometries of interest are coated metallic spheres and cylinders and homogeneous chiral spheres and cylinders. The interplay of these geometries with electromagnetic chirality and their joint effect on depolarization are analyzed. Of interest are the physical principles of electromagnetic chirality involved with angular scattering and the relative effects of curvature, loss, and degree of chirality. The dependence of Mueller matrices on chirality is investigated

in a first step toward remote sensing and characterization of chiral coated particles from angular scattering measurements.

Selected work in electromagnetic chirality includes scattering from chiral objects with planar [3–6], cylindrical [7–10], spherical [7,11–14], ellipsoidal [15] and wire geometries [16,17]. Most of this work has concentrated on backscatter and total scatter cross-sections. Here the differential scattering cross-sections are examined.

In the following sections, a mathematical description of waves in chiral media is given and the eigenmode expansions for layered cylindrical and spherical geometries are formulated. The scattering cross-sections and Mueller matrices for a chiral coated metallic cylinder and sphere are determined and compared through a coordinated set of examples.

2. Electromagnetic Chirality and Curved Geometries

Chirality refers to the lack of bilateral symmetry in an object, and chiral structures can be classified as either right or left handed. A collection of chiral structures of a similar handedness forms a chiral material. Such materials possess an intrinsic handedness due to their microscopic composition. An isotropic, reciprocal chiral medium can be described by the set of generalized constitutive relations, $\mathbf{D} = \varepsilon\mathbf{E} + i\xi_c\mathbf{B}$ and $\mathbf{H} = i\xi_c\mathbf{E} + (1/\mu)\mathbf{B}$ where $\mathbf{E}, \mathbf{B}, \mathbf{D}$ and $\mathbf{H}$ are the usual electromagnetic field vectors [1]. The permeability and permittivity are represented by μ and ε, respectively, and the chirality admittance ξ_c is a quantity introduced to incorporate the effects of chirality. In particular, ξ_c is a measure of the degree of chirality of the medium through its magnitude. The sign of ξ_c specifies the medium handedness.

From the generalized chiral constitutive relations and the time-harmonic Maxwell's equations for $(e^{-i\omega t})$ excitation, the chiral Helmholtz equation in a sourceless region is found to be,

$$\nabla \times \nabla \times \mathbf{C} - 2\omega\mu\xi_c \nabla \times \mathbf{C} - \omega^2\mu\varepsilon\mathbf{C} = 0 \tag{1}$$

where $\mathbf{C}$ is any of the electromagnetic field vectors and $k(= \omega\sqrt{\mu\varepsilon})$ the intrinsic wavenumber of the medium. From this equation, it is found that propagating eigenmodes within such media consist of two circularly-polarized waves with characteristic wavenumbers, $k_\pm =$

$2\pi/\lambda_{\pm} = \pm\omega\mu\xi_c + \sqrt{k^2 + (\omega\mu\xi_c)^2}$. Here, the + and – subscripts denote the right circularly polarized (RCP) and left circularly polarized (LCP) modes, respectively.

Seeking to scalarize the chiral Helmholtz equation, a set of vector wave functions is formulated to characterize waves within the chiral layer. The classical eigenmodes $\mathbf{m}(\mathrm{k})$ and $\mathbf{n}(\mathrm{k})$ [18] of the achiral Helmholtz equation, however, do not satisfy this equation due to the second curl term in (1). Instead, a linear combination is taken to form a new set of chiral eigenfunctions,

$$\left\{ \begin{array}{c} \mathbf{A}(k) \\ \mathbf{B}(k) \end{array} \right\} = \frac{1}{\sqrt{2}} \Big[\mathbf{m}(k) \pm \mathbf{n}(k) \Big]. \tag{2}$$

These new wave functions are unaltered by the curl operator,

$$\nabla \times \left\{ \begin{array}{c} \mathbf{A}(k) \\ \mathbf{B}(k) \end{array} \right\} = \pm k \left\{ \begin{array}{c} \mathbf{A}(k) \\ \mathbf{B}(k) \end{array} \right\} \tag{3}$$

and therefore satisfy the chiral Helmholtz equation (1). This is a generalization of the circularly polarized eigenmodes of the planar case and this concept is applicable for any of the separable coordinate systems.

2.1 Cylindrical Layers

Consider the problem geometry of Fig. 1a. A plane wave traveling in free space is incident on a perfectly conducting metal cylinder of radius a, upon which a chiral layer of thickness Δ has been placed. The chiral layer is characterized by a chiral impedance η_c and wavenumbers k_+ and k_-.

From the classical cylindrical eigenmodes $\mathbf{m}_n(k)$ and $\mathbf{n}_n(k)$, a set of chiral wave functions can be constructed of the form,

$$\left\{ \begin{array}{c} \mathbf{A}_n^{(q)}(k) \\ \mathbf{B}_n^{(q)}(k) \end{array} \right\} = \\ \frac{1}{\sqrt{2}} \left[\frac{in}{\rho} Z_n(k\rho) e^{in\phi} \hat{\mathbf{e}}_\rho - \frac{\partial Z_n(k\rho)}{\partial \rho} e^{in\phi} \hat{\mathbf{e}}_\phi \pm k Z_n(k\rho) e^{in\phi} \hat{\mathbf{e}}_z \right] \tag{4}$$

where $q = 1, 2, 3, 4$ indicates that $Z_n(k\rho)$ becomes one of the Bessel functions $J_n(k\rho), Y_n(k\rho), H_n^{(1)}(k\rho)$, and $H_n^{(2)}(k\rho)$, respectively. Here

$\hat{\mathbf{e}}_\rho, \hat{\mathbf{e}}_\phi$, and $\hat{\mathbf{e}}_z$ are unit vectors. These functions determine the cross-polar ($\mathbf{r}_n^{ab}$ and $\mathbf{r}_n^{ba}$) and co-polar ($\mathbf{r}_n^{aa}$ and $\mathbf{r}_n^{bb}$) angular scattering coefficients of the coated cylinder (see Appendix).

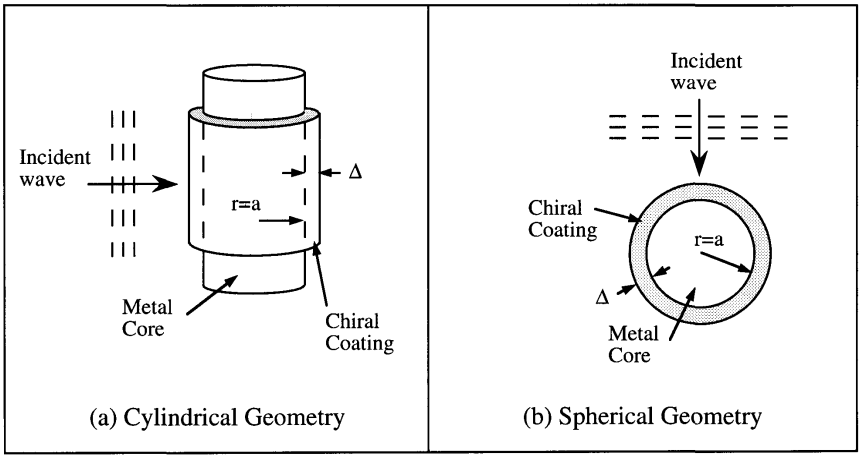

Figure 1. Scattering geometry.

The cylindrical wave function expansion of an incident RCP plane wave is given by,

$$\mathbf{E}_+^i = \hat{\mathbf{e}}_+ e^{ik_0 x} = \left(\frac{\hat{\mathbf{e}}_y + i\hat{\mathbf{e}}_z}{\sqrt{2}} \right) e^{ik_0 x} = \frac{i}{k_0} \sum_{n=-\infty}^{\infty} i^n \mathbf{A}_n^{(1)}(k_0). \qquad (5)$$

The scattered field due to this wave is expressed by,

$$\mathbf{E}_+^r = \frac{i}{k_0} \sum_{n=-\infty}^{\infty} i^n \left[\mathbf{r}_n^{aa} \mathbf{A}_n^{(3)}(k_0) + \mathbf{r}_n^{ab} \mathbf{B}_n^{(3)}(k_0) \right]. \qquad (6)$$

Taking the large argument approximations for the Bessel functions, the chiral cylindrical vector wave functions reduce in the far-field regime to,

$$\left\{ \begin{array}{c} \mathbf{A}_n^{(3)}(k_0) \\ \mathbf{B}_n^{(3)}(k_0) \end{array} \right\} = -(1+i) \sqrt{\frac{k_0}{2\pi\rho}} (-i)^n e^{ik_0\rho} e^{in\phi} \left(\hat{\mathbf{e}}_\phi \pm i\hat{\mathbf{e}}_z \right). \qquad (7)$$

The scattered field becomes,

$$\mathbf{E}_{+}^{r} = (1-i)\sqrt{\frac{1}{2\pi k_0 \rho}} e^{ik_0\rho} \sum_{n=-\infty}^{\infty} \left[\mathbf{r}_n^{aa}(\hat{\mathbf{e}}_\phi + i\hat{\mathbf{e}}_z) + \mathbf{r}_n^{ab}(\hat{\mathbf{e}}_\phi - i\hat{\mathbf{e}}_z) \right] e^{in\phi}. \quad (8)$$

The co-polar (RCP $\rightarrow$ RCP) and cross-polar (RCP $\rightarrow$ LCP) differential scattering cross-sections per unit length are defined as,

$$\left.\frac{d\sigma}{d\phi}\right|_{RCP\rightarrow RCP} = \lim_{\rho\to\infty} \rho \frac{|\hat{\mathbf{e}}_{+}^{r*} \bullet \mathbf{E}_{+}^{r}|^2}{|\hat{\mathbf{e}}_{+}^{*} \bullet \mathbf{E}_{+}^{i}|^2} = \frac{2}{\pi k_0} \left| \sum_{n=1}^{\infty} \mathbf{r}_n^{aa} e^{in\phi} \right|^2 \quad (9)$$

$$\left.\frac{d\sigma}{d\phi}\right|_{RCP\rightarrow LCP} = \lim_{\rho\to\infty} \rho \frac{|\hat{\mathbf{e}}_{-}^{r*} \bullet \mathbf{E}_{+}^{r}|^2}{|\hat{\mathbf{e}}_{+}^{*} \bullet \mathbf{E}_{+}^{i}|^2} = \frac{2}{\pi k_0} \left| \sum_{n=1}^{\infty} \mathbf{r}_n^{ab} e^{in\phi} \right|^2 \quad (10)$$

with

$$\hat{\mathbf{e}}_{\pm}^{r} = \frac{\hat{\mathbf{e}}_\phi \pm i\hat{\mathbf{e}}_z}{\sqrt{2}}. \quad (11)$$

For an incident LCP plane wave, the cylindrical expansion is given by

$$\mathbf{E}_{-}^{i} = \hat{\mathbf{e}}_{-} e^{ik_0 x} = \left(\frac{\hat{\mathbf{e}}_y - i\hat{\mathbf{e}}_z}{\sqrt{2}} \right) e^{ik_0 x} = \frac{i}{k_0} \sum_{n=-\infty}^{\infty} i^n \mathbf{B}_n^{(1)}(k_0) \quad (12)$$

and the far-zone scattered field is written,

$$\mathbf{E}_{-}^{r} = (1-i)\sqrt{\frac{1}{2\pi k_0 \rho}} e^{ik_0\rho} \sum_{n=-\infty}^{\infty} \left[\mathbf{r}_n^{ba}(\hat{\mathbf{e}}_\phi + i\hat{\mathbf{e}}_z) + \mathbf{r}_n^{bb}(\hat{\mathbf{e}}_\phi - i\hat{\mathbf{e}}_z) \right] e^{in\phi}. \quad (13)$$

The cross-polar (LCP $\rightarrow$ RCP) and co-polar (LCP $\rightarrow$ LCP) differential scattering cross-sections per unit length are given by,

$$\left.\frac{d\sigma}{d\phi}\right|_{LCP\rightarrow RCP} = \lim_{\rho\to\infty} \rho \frac{\left|\hat{\mathbf{e}}_{+}^{r*} \bullet \mathbf{E}_{-}^{r}\right|^2}{\left|\hat{\mathbf{e}}_{-}^{*} \bullet \mathbf{E}_{-}^{i}\right|^2} = \frac{2}{\pi k_0} \left| \sum_{n=1}^{\infty} \mathbf{r}_n^{ba} e^{in\phi} \right|^2 \quad (14)$$

$$\left.\frac{d\sigma}{d\phi}\right|_{LCP\to LCP} = \lim_{\rho\to\infty}\rho\frac{\left|\hat{\mathbf{e}}_-^{r*}\bullet\mathbf{E}_-^r\right|^2}{\left|\hat{\mathbf{e}}_-^{*}\bullet\mathbf{E}_-^i\right|^2} = \frac{2}{\pi k_0}\left|\sum_{n=1}^{\infty}\mathbf{r}_n^{bb}e^{in\phi}\right|^2. \qquad (15)$$

The spherical case is treated in the same manner in the next section. The four relations (9), (10), (14), and (15) are used in the examples of section III.

2.2 Spherical Layers

Consider Fig. 1b, where a plane wave is incident upon a perfectly conducting sphere of radius a coated with a spherical chiral layer of thickness Δ. The chiral layer is characterized by a chiral impedance η_c and wavenumbers k_+ and k_-.

From the orthogonal spherical eigenmodes $\mathbf{m}_{\substack{e\\o}mn}(k)$ and $\mathbf{n}_{\substack{e\\o}mn}(k)$, the chiral wave functions are constructed. They are given by,

$$\begin{aligned}
&\left\{\begin{matrix}\mathbf{A}^{(q)}_{\substack{e\\o}mn}(k)\\ \mathbf{B}^{(q)}_{\substack{e\\o}mn}(k)\end{matrix}\right\}\\
&= \frac{1}{\sqrt{2}}\left[\frac{m}{\sin\theta}P_n^m(\cos\theta)\left\{\begin{matrix}-\sin\\+\cos\end{matrix}\right\}(m\phi)\left(z_n(kr)\hat{\mathbf{e}}_\theta \pm \frac{1}{kr}\frac{\partial}{\partial r}[rz_n(kr)]\hat{\mathbf{e}}_\phi\right)\right.\\
&\quad + \frac{\partial P_n^m(\cos\theta)}{\partial\theta}\left\{\begin{matrix}\cos\\\sin\end{matrix}\right\}(m\phi)\left(\pm\frac{1}{kr}\frac{\partial}{\partial r}[rz_n(kr)]\hat{\mathbf{e}}_\theta - z_n(kr)\hat{\mathbf{e}}_\phi\right)\\
&\quad \left.\pm n(n+1)P_n^m(\cos\theta)\left\{\begin{matrix}\cos\\\sin\end{matrix}\right\}(m\phi)\frac{z_n(kr)}{kr}\hat{\mathbf{e}}_r\right]
\end{aligned} \qquad (16)$$

where $q = 1,2,3,4$, indicates that $z_n(kr)$ represents the spherical Bessel functions $j_n(kr), y_n(kr)$, $h_n^{(1)}(kr)$ and $h_n^{(2)}(kr)$, respectively, and where $\hat{\mathbf{e}}_\theta$, $\hat{\mathbf{e}}_\phi$, and $\hat{\mathbf{e}}_r$ are unit vectors. Here, $P_n^m(\cos\theta)$ is an associated Legendre function of order m and degree n. These wave functions can be utilized to find the cross-polar (Γ_{mn}^{ab} and Γ_{mn}^{ba}) and co-polar (Γ_{mn}^{aa} and Γ_{mn}^{bb}) scattering coefficients for the coated metallic sphere (see Appendix).

The spherical wave function expansion of an incident RCP plane wave is given by,

$$\mathbf{E}_+^i = \hat{\mathbf{e}}_+ e^{ik_0 z} = \left(\frac{\hat{\mathbf{e}}_x + i\hat{\mathbf{e}}_y}{\sqrt{2}}\right) e^{ik_0 z} = \sum_{n=1}^{\infty} i^n \frac{2n+1}{n(n+1)} \left[\mathbf{A}_{o1n}^{(1)}(k_0) - i\mathbf{A}_{e1n}^{(1)}(k_0)\right]. \quad (17)$$

If this wave were incident on the coated sphere, the scattered field can be found directly from the above results to be,

$$\mathbf{E}_+^r = \sum_{n=1}^{\infty} i^n \frac{2n+1}{n(n+1)} \left[\Gamma_{1n}^{aa}\mathbf{A}_{o1n}^{(3)}(k_0) + \Gamma_{1n}^{ab}\mathbf{B}_{o1n}^{(3)}(k_0) - i\left\{\Gamma_{1n}^{aa}\mathbf{A}_{e1n}^{(3)}(k_0) + \Gamma_{1n}^{ab}\mathbf{B}_{e1n}^{(3)}(k_0)\right\}\right]. \quad (18)$$

To determine the differential scattering cross-sections, the spherical Bessel functions are replaced by their far-field approximations. The chiral wave functions reduce to,

$$\left\{\begin{array}{c}\mathbf{A}_{e1n}^{(3)}(k_0)\\ \mathbf{B}_{e1n}^{(3)}(k_0)\end{array}\right\} = (-i)^n \frac{e^{ik_0 r}}{k_0 r}\left[\frac{iP_n^1(\cos\theta)}{\sin\theta}\sin\phi \pm \frac{\partial P_n^1(\cos\theta)}{\partial\theta}\cos\phi\right]\frac{(\hat{\mathbf{e}}_\theta \pm i\hat{\mathbf{e}}_\phi)}{\sqrt{2}} \quad (19)$$

$$\left\{\begin{array}{c}\mathbf{A}_{o1n}^{(3)}(k_0)\\ \mathbf{B}_{o1n}^{(3)}(k_0)\end{array}\right\} = (-i)^n \frac{e^{ik_0 r}}{k_0 r}\left[\pm\frac{\partial P_n^1(\cos\theta)}{\partial\theta}\sin\phi - \frac{iP_n^1(\cos\theta)}{\sin\theta}\cos\phi\right]\frac{(\hat{\mathbf{e}}_\theta \pm i\hat{\mathbf{e}}_\phi)}{\sqrt{2}} \quad (20)$$

and the far-zone scattered field is written,

$$\mathbf{E}_{+}^{r} = \frac{i}{\sqrt{2}}\frac{e^{ik_0 r}}{k_0 r}e^{i\phi}\sum_{n=1}^{\infty}\frac{2n+1}{n(n+1)} \left\{\Gamma_{1n}^{aa}\left[\frac{P_n^1(\cos\theta)}{\sin\theta}+\frac{\partial P_n^1(\cos\theta)}{\partial\theta}\right](\hat{\mathbf{e}}_\theta + i\hat{\mathbf{e}}_\phi) + \Gamma_{1n}^{ab}\left[\frac{P_n^1(\cos\theta)}{\sin\theta}-\frac{\partial P_n^1(\cos\theta)}{\partial\theta}\right](\hat{\mathbf{e}}_\theta - i\hat{\mathbf{e}}_\phi)\right\}. \tag{21}$$

The co-polar (RCP $\rightarrow$ RCP) and cross-polar (RCP $\rightarrow$ LCP) differential scattering cross-sections are defined as,

$$\left.\frac{d\sigma}{d\Omega}\right|_{RCP\rightarrow RCP} = \lim_{r\rightarrow\infty} r^2\frac{|\hat{\mathbf{e}}_{+}^{r*}\bullet\mathbf{E}_{+}^{r}|^2}{|\hat{\mathbf{e}}_{+}^{*}\bullet\mathbf{E}_{+}^{i}|^2} = \frac{1}{k_0^2}\left|\sum_{n=1}^{\infty}\frac{2n+1}{n(n+1)}\left[\frac{P_n^1(\cos\theta)}{\sin\theta}+\frac{\partial P_n^1(\cos\theta)}{\partial\theta}\right]\Gamma_{1n}^{aa}\right|^2 \tag{22}$$

$$\left.\frac{d\sigma}{d\Omega}\right|_{RCP\rightarrow LCP} = \lim_{r\rightarrow\infty} r^2\frac{|\hat{\mathbf{e}}_{-}^{r*}\bullet\mathbf{E}_{+}^{r}|^2}{|\hat{\mathbf{e}}_{+}^{*}\bullet\mathbf{E}_{+}^{i}|^2} = \frac{1}{k_0^2}\left|\sum_{n=1}^{\infty}\frac{2n+1}{n(n+1)}\left[\frac{P_n^1(\cos\theta)}{\sin\theta}-\frac{\partial P_n^1(\cos\theta)}{\partial\theta}\right]\Gamma_{1n}^{ab}\right|^2 \tag{23}$$

with

$$\hat{\mathbf{e}}_{\pm}^{r} = \frac{\hat{\mathbf{e}}_\theta \pm i\hat{\mathbf{e}}_\phi}{\sqrt{2}}. \tag{24}$$

For an incident LCP plane wave, the spherical expansion is given by,

$$\mathbf{E}_{-}^{i} = \hat{e}_{-}e^{ik_0 z} = \left(\frac{\hat{\mathbf{e}}_x - i\hat{\mathbf{e}}_y}{\sqrt{2}}\right)e^{ik_0 z} = \sum_{n=1}^{\infty} i^n\frac{2n+1}{n(n+1)}\left[\mathbf{B}_{o1n}^{(1)}(k_0) + i\mathbf{B}_{e1n}^{(1)}(k_0)\right] \tag{25}$$

and the far-zone scattered field is written,

$$\mathbf{E}_{-}^{r} = \frac{i}{\sqrt{2}} \frac{e^{ik_0 r}}{k_0 r} \sum_{n=1}^{\infty} \frac{2n+1}{n(n+1)} \left\{ \Gamma_{1n}^{ba} \left[\frac{P_n^1(\cos\theta)}{\sin\theta} - \frac{\partial P_n^1(\cos\theta)}{\partial\theta} \right] (\hat{\mathbf{e}}_\theta + i\hat{\mathbf{e}}_\phi) \right. \\ \left. \Gamma_{1n}^{bb} \left[\frac{P_n^1(\cos\theta)}{\sin\theta} + \frac{\partial P_n^1(\cos\theta)}{\partial\theta} \right] (\hat{\mathbf{e}}_\theta - i\hat{\mathbf{e}}_\phi) \right\} \quad (26)$$

with the following definitions for the cross-polar (LCP $\rightarrow$ RCP) and co-polar (LCP $\rightarrow$ LCP) differential scattering cross-sections,

$$\left.\frac{d\sigma}{d\Omega}\right|_{LCP\rightarrow RCP} = \lim_{r\rightarrow\infty} r^2 \frac{|\hat{\mathbf{e}}_{+}^{r*} \bullet \mathbf{E}_{-}^{r}|^2}{|\hat{\mathbf{e}}_{-}^{*} \bullet \mathbf{E}_{-}^{i}|^2} \\ = \frac{1}{k_0^2} \left| \sum_{n=1}^{\infty} \frac{2n+1}{n(n+1)} \left[\frac{P_n^1(\cos\theta)}{\sin\theta} - \frac{\partial P_n^1(\cos\theta)}{\partial\theta} \right] \Gamma_{1n}^{ba} \right|^2 \quad (27)$$

$$\left.\frac{d\sigma}{d\Omega}\right|_{LCP\rightarrow LCP} = \lim_{r\rightarrow\infty} r^2 \frac{|\hat{\mathbf{e}}_{-}^{r*} \bullet \mathbf{E}_{-}^{r}|^2}{|\hat{\mathbf{e}}_{-}^{*} \bullet \mathbf{E}_{-}^{i}|^2} \\ = \frac{1}{k_0^2} \left| \sum_{n=1}^{\infty} \frac{2n+1}{n(n+1)} \left[\frac{P_n^1(\cos\theta)}{\sin\theta} + \frac{\partial P_n^1(\cos\theta)}{\partial\theta} \right] \Gamma_{1n}^{bb} \right|^2 . \quad (28)$$

The four relations (22), (23), (27), and (28) are used in the examples of the next section.

3. Examples and Results

The differential scattering cross-sections for the chiral coated conducting cylinder and sphere are plotted in Figs. 2, 3, and 4 for the lossless, lossy permittivity, and lossy permeability cases, respectively. The top, middle, and bottom plots correspond to chirality admittances

of $\eta_0\xi_c = 0.0, 0.5,$ and 1.0. In the lossless case of Fig. 2, the permeability of the layer is that of free space $\mu = \mu_0$ and the permittivity is $\varepsilon = 4\varepsilon_0$. In Fig. 3, the permeability is $\mu = \mu_0$ and the permittivity is $\varepsilon = (4 + i2)\varepsilon_0$. This corresponds to a loss ratio of $\varepsilon_i/\varepsilon_r = 0.5$. In Fig. 4, $\mu = (2 + i)\mu_0$ and $\varepsilon = 2\varepsilon_0$. This again corresponds to a loss ratio of $\mu_i/\mu_r = 0.5$. In all figures, the radius of the conducting cylinder or sphere is $a = \lambda$ (where λ is the wavelength associated with the incident wave frequency) and the thickness of the chiral coating is $\Delta = 0.5\lambda$.

We can understand the results of Figs. 2–4 by investigating the effects of geometry and chirality separately. For the sphere in the backscatter direction, no co-polar scattering occurs, and in the forward scatter direction, no cross-polar scattering occurs. This agrees with our physical reasoning since neither the geometry nor the reciprocal nature of the medium provide the necessary coupling mechanism for co-polar backscattering or cross-polar forward scattering. To see the effect of geometry, consider the equations for the differential scattering cross-sections. In backscatter $(\theta = \pi)$, the Legendre functions reduce to,

$$\left.\frac{P_n^1(\cos\theta)}{\sin\theta}\right|_{\theta=\pi} = -\left.\frac{\partial P_n^1(\cos\theta)}{\partial\theta}\right|_{\theta=\pi} = (-1)^n\frac{n(n+1)}{2}. \tag{29}$$

Thus, the co-polar scattering cross-sections (RCP $\rightarrow$ RCP and LCP $\rightarrow$ LCP) are identically zero. Similarly, in forward scatter $(\theta = 0)$, we have,

$$\left.\frac{P_n^1(\cos\theta)}{\sin\theta}\right|_{\theta=0} = \left.\frac{\partial P_n^1(\cos\theta)}{\partial\theta}\right|_{\theta=0} = (-1)^n\frac{n(n+1)}{2} \tag{30}$$

and no cross-polar scattering (RCP $\rightarrow$ LCP and LCP $\rightarrow$ RCP) occurs. This result is not true for the cylinder, where the geometry will inherently depolarize all scattered waves. This is because of the asymmetry of the cylinder due to the presence of a preferred geometrical axis.

Several conclusions regarding the effect of chirality on angular scattering can be made from the figures. As chirality is increased, the co-polar scattering cross-sections are split. This circular birefringence is a consequence of the different wavenumbers of RCP and LCP waves in the chiral layer. Waves of each handedness "see" a scatterer of different size, as evident in the resonance behavior of the co-polar scattering cross-sections.

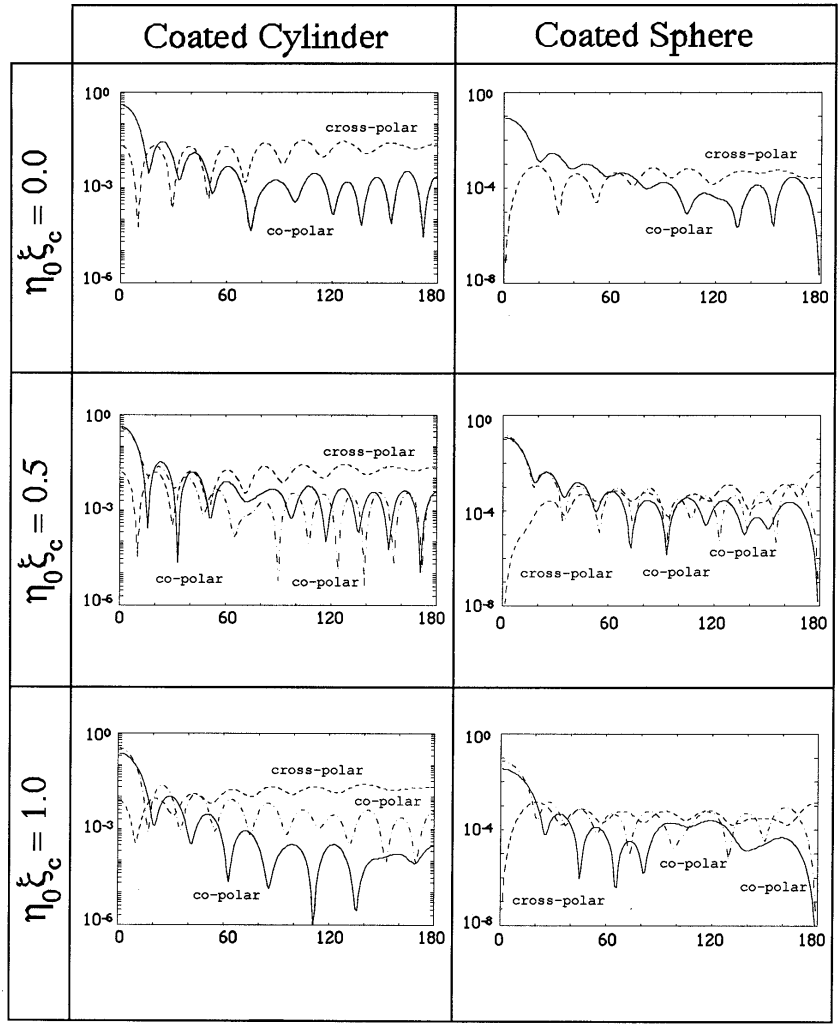

Figure 2. Differential scattering cross-sections for the chiral coated conducting cylinder and sphere plotted as a function of scattering angle (lossless case).

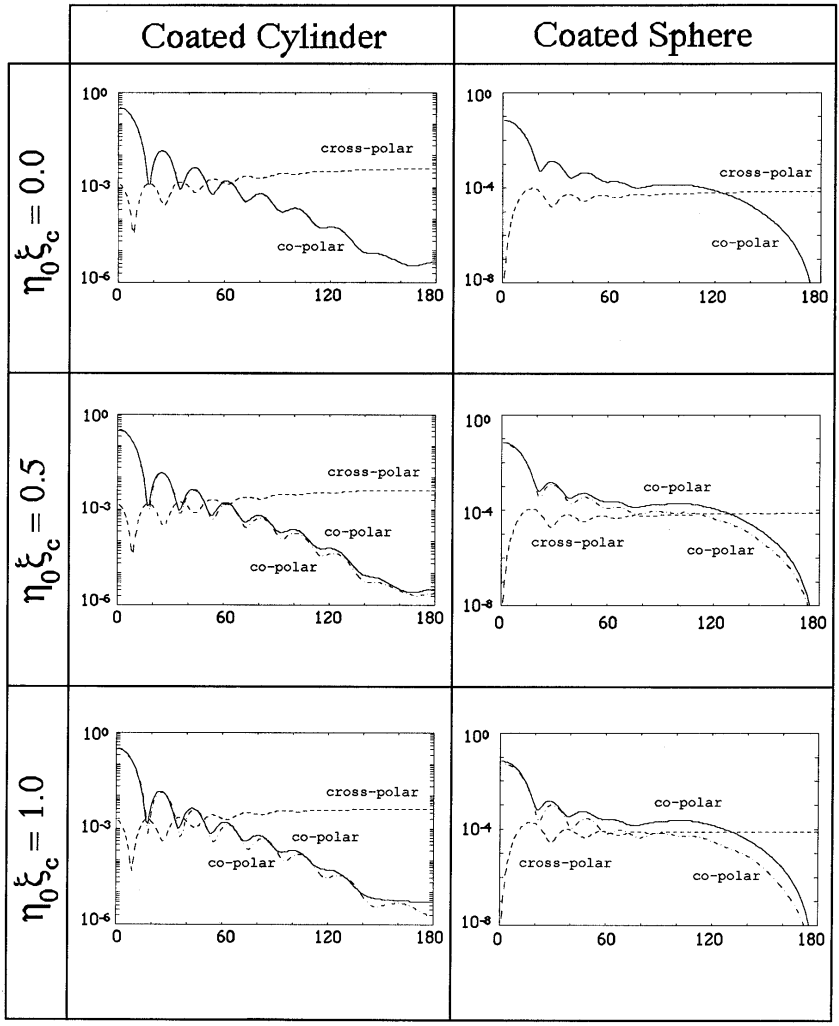

Figure 3. Differential scattering cross-sections for the chiral coated conducting cylinder and sphere plotted as a function of scattering angle (lossy permittivity case).

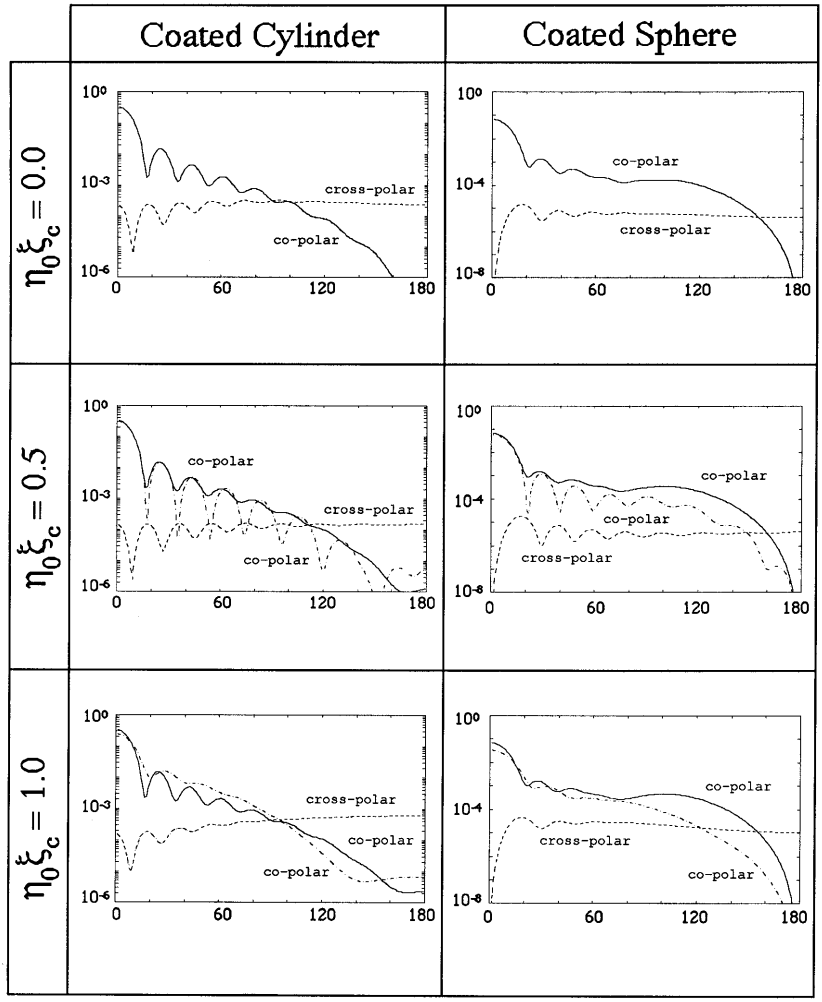

Figure 4. Differential scattering cross-sections for the chiral coated conducting cylinder and sphere as a function of scattering angle (lossy permeability case).

For the cross-polar scattering cross-sections, no splitting is evident. Rather, chirality modifies the magnitude of these cross-sections. Due to the reciprocity of the medium, waves within the layer travel equal distances with each handedness for cross-polar scattering and therefore no distinction exists between RCP $\rightarrow$ LCP and LCP $\rightarrow$ RCP scattering. The addition of chirality, in this case, acts in two ways on the scattering behavior. Waves see both a new effective wavenumber $k_c = (k_+ + k_-)/2$ and impedance $\eta_c = \omega\mu/k_c$ in the chiral layer. The first effect modifies the resonance behavior while the second effect changes the amplitude of scattering due to front-surface impedance mismatch.

Losses in both permittivity and permeability tend to dampen the resonance structures of the scattering cross-sections as expected from physical considerations. In addition, the splitting of the co-polar scattering cross-sections is more easily discerned with increasing loss. For equal loss ratios in ε and μ, however, we see that the effect of losses in permeability is greater with increasing chirality. Thus, chirality acts to intensify effective permeability losses within the coating. This can be deduced from the form of the chiral wavenumbers, which clearly indicate the linking of permeability losses to overall loss through the $\pm\omega\mu\xi_c$ term. This magnification is not equal for the two co-polar scattering cross-sections, since RCP and LCP waves possess different wavenumbers and experience different losses within the coating. Figure 4 clearly depicts this circular dichroism.

It is observed that the results of the backscatter case in the figures are very similar to that of the planar case [5]. In general, the backscatter results can be predicted from an extension of planar results when the radius a of the scatterer is on the order of $a \gtrsim \lambda$.

The Mueller matrix defines the relation between the Stokes parameters of an incident wave and those of a scattered wave. For circular polarization, the four Stokes parameters are written,

$$\begin{aligned}
S_0 &= (\hat{\mathbf{e}}_+^* \bullet \mathbf{E})^*(\hat{\mathbf{e}}_+^* \bullet \mathbf{E}) + (\hat{\mathbf{e}}_-^* \bullet \mathbf{E})^*(\hat{\mathbf{e}}_-^* \bullet \mathbf{E}) \\
S_1 &= (\hat{\mathbf{e}}_+^* \bullet \mathbf{E})^*(\hat{\mathbf{e}}_-^* \bullet \mathbf{E}) + (\hat{\mathbf{e}}_-^* \bullet \mathbf{E})^*(\hat{\mathbf{e}}_+^* \bullet \mathbf{E}) \\
S_2 &= (\hat{\mathbf{e}}_+^* \bullet \mathbf{E})^*(\hat{\mathbf{e}}_-^* \bullet \mathbf{E}) - (\hat{\mathbf{e}}_-^* \bullet \mathbf{E})^*(\hat{\mathbf{e}}_+^* \bullet \mathbf{E}) \\
S_3 &= (\hat{\mathbf{e}}_+^* \bullet \mathbf{E})^*(\hat{\mathbf{e}}_+^* \bullet \mathbf{E}) - (\hat{\mathbf{e}}_-^* \bullet \mathbf{E})^*(\hat{\mathbf{e}}_-^* \bullet \mathbf{E})
\end{aligned} \tag{31}$$

where

$$\hat{\mathbf{e}}_+^* \bullet \mathbf{E} = \sum_{n=1}^{\infty} \mathbf{r}_n^{aa} e^{in\phi} + \sum_{n=1}^{\infty} \mathbf{r}_n^{ba} e^{in\phi} \tag{32}$$

$$\hat{\mathbf{e}}_-^* \bullet \mathbf{E} = \sum_{n=1}^{\infty} \mathbf{r}_n^{ab} e^{in\phi} + \sum_{n=1}^{\infty} \mathbf{r}_n^{bb} e^{in\phi} \tag{33}$$

for the cylindrical case and

$$\begin{aligned}\hat{\mathbf{e}}_+^* \bullet \mathbf{E} = &\sum_{n=1}^{\infty} \frac{2n+1}{n(n+1)} \Gamma_{1n}^{aa} \left[\frac{P_n^1(\cos\theta)}{\sin\theta} + \frac{\partial P_n^1(\cos\theta)}{\partial\theta} \right] \\ &+ \sum_{n=1}^{\infty} \frac{2n+1}{n(n+1)} \Gamma_{1n}^{ab} \left[\frac{P_n^1(\cos\theta)}{\sin\theta} - \frac{\partial P_n^1(\cos\theta)}{\partial\theta} \right]\end{aligned} \tag{34}$$

$$\begin{aligned}\hat{\mathbf{e}}_-^* \bullet \mathbf{E} = &\sum_{n=1}^{\infty} \frac{2n+1}{n(n+1)} \Gamma_{1n}^{ba} \left[\frac{P_n^1(\cos\theta)}{\sin\theta} - \frac{\partial P_n^1(\cos\theta)}{\partial\theta} \right] \\ &+ \sum_{n=1}^{\infty} \frac{2n+1}{n(n+1)} \Gamma_{1n}^{bb} \left[\frac{P_n^1(\cos\theta)}{\sin\theta} + \frac{\partial P_n^1(\cos\theta)}{\partial\theta} \right]\end{aligned} \tag{35}$$

for the spherical case. The Mueller matrix is given by,

$$\begin{bmatrix} S_0^r \\ S_1^r \\ S_2^r \\ S_3^r \end{bmatrix} = \begin{bmatrix} M_{11} & M_{12} & M_{13} & M_{14} \\ M_{21} & M_{22} & M_{23} & M_{24} \\ M_{31} & M_{32} & M_{33} & M_{34} \\ M_{41} & M_{42} & M_{43} & M_{44} \end{bmatrix} \begin{bmatrix} S_0^i \\ S_1^i \\ S_2^i \\ S_3^i \end{bmatrix}. \tag{36}$$

The elements of the Mueller scattering matrix are plotted in Figs. 5 and 6 for a representative coated conducting cylinder and sphere as a function of scattering angle. The coating has a thickness $\Delta = 0.5\lambda$, a permeability $\mu = 2\mu_0$, and a permittivity $\varepsilon = 4\varepsilon_0$. The radius of the conducting cylinder and sphere is $a = \lambda$. In each plot, the solid and dotted lines correspond to the chiral and achiral layer cases ($\eta_0\xi_c = 1.0$), respectively. In the achiral case, the symmetry of the matrix is clearly evident and given explicitly by

$$M_{13} = M_{14} = M_{23} = M_{24} = 0 \tag{37}$$

$$M_{44} = M_{33} \qquad \text{and} \qquad M_{22} = M_{11}. \tag{38}$$

The symmetry about the main diagonal is due to the reciprocity and random orientation of particles within the chiral medium. This implies that only four independent parameters exist, in accordance with the predictions of Perrin [19] and Van de Hulst [20] for a distribution of identical particles in random orientation under circular polarization. The depolarization effect of the cylindrical geometry is again evident from the off-diagonal Mueller matrix elements, which exhibit nulls for the spherical case in either the forward or backscattering direction but not for the cylindrical case.

The addition of electromagnetic chirality manifests itself in two forms. The first is in the variation in magnitude and resonance behavior of the matrix element plots. Here, RCP and LCP waves see chiral coatings of different thickness and impedance. This causes a shift of the nulls in each of the matrix plots. The second manifestation of chirality is observed in the Mueller matrix elements M_{31}, M_{32}, M_{41}, and M_{42} of Figs. 5 and 6. When chirality is present, these elements are non-zero and satisfy the conditions

$$M_{31} = M_{13}, \qquad M_{32} = M_{23}, \qquad M_{41} = M_{14}, \qquad M_{42} = M_{24}. \tag{39}$$

Based on these relationships, only 10 independent elements exist in the Mueller matrices, agreeing with Perrin's results [19] for a distribution of asymmetric particles of one handedness with random orientation.

The total power of the four most sensitive Mueller matrix elements are calculated by integrating them over angle,

$$K_{31} = \int_0^{2\pi} M_{31}(\alpha)d\alpha \qquad K_{32} = \int_0^{2\pi} M_{32}(\alpha)d\alpha \tag{40}$$

$$K_{41} = \int_0^{2\pi} M_{41}(\alpha)d\alpha \qquad K_{42} = \int_0^{2\pi} M_{42}(\alpha)d\alpha \tag{41}$$

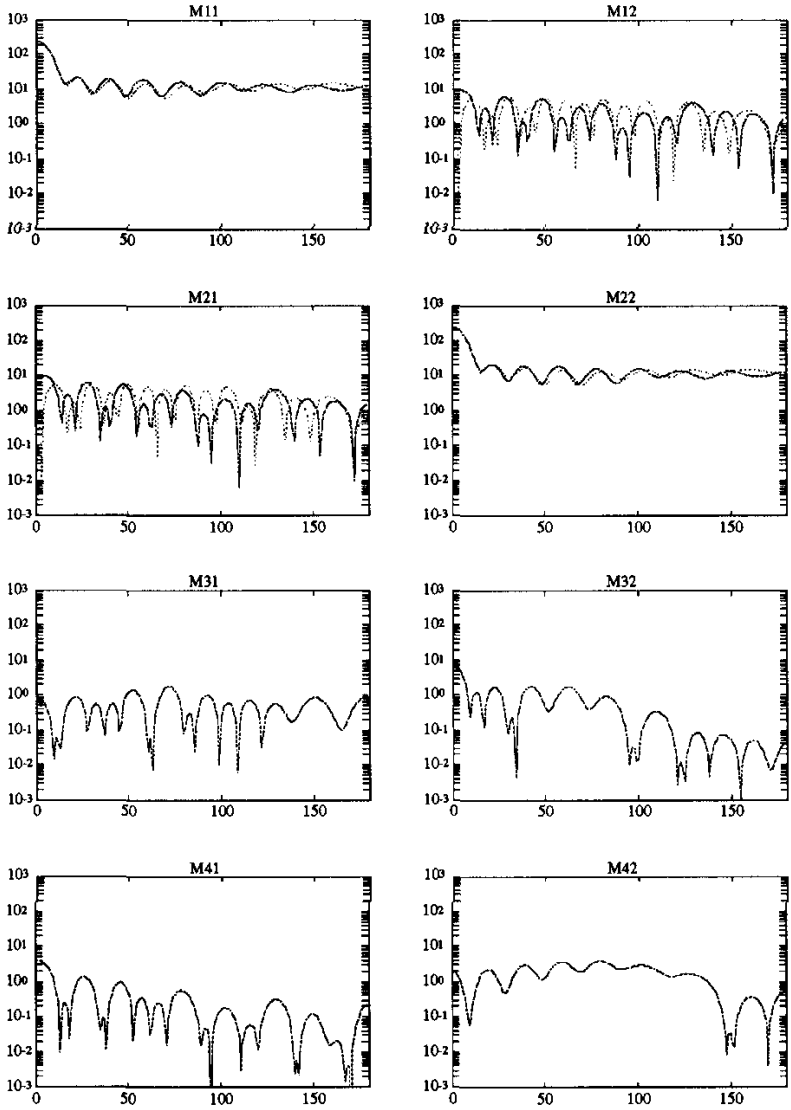

Figure 5. Elements of the Mueller scattering matrix plotted for the coated conducting cylinder as a function of scattering angle (dotted line = achiral case, solid line = chiral case).

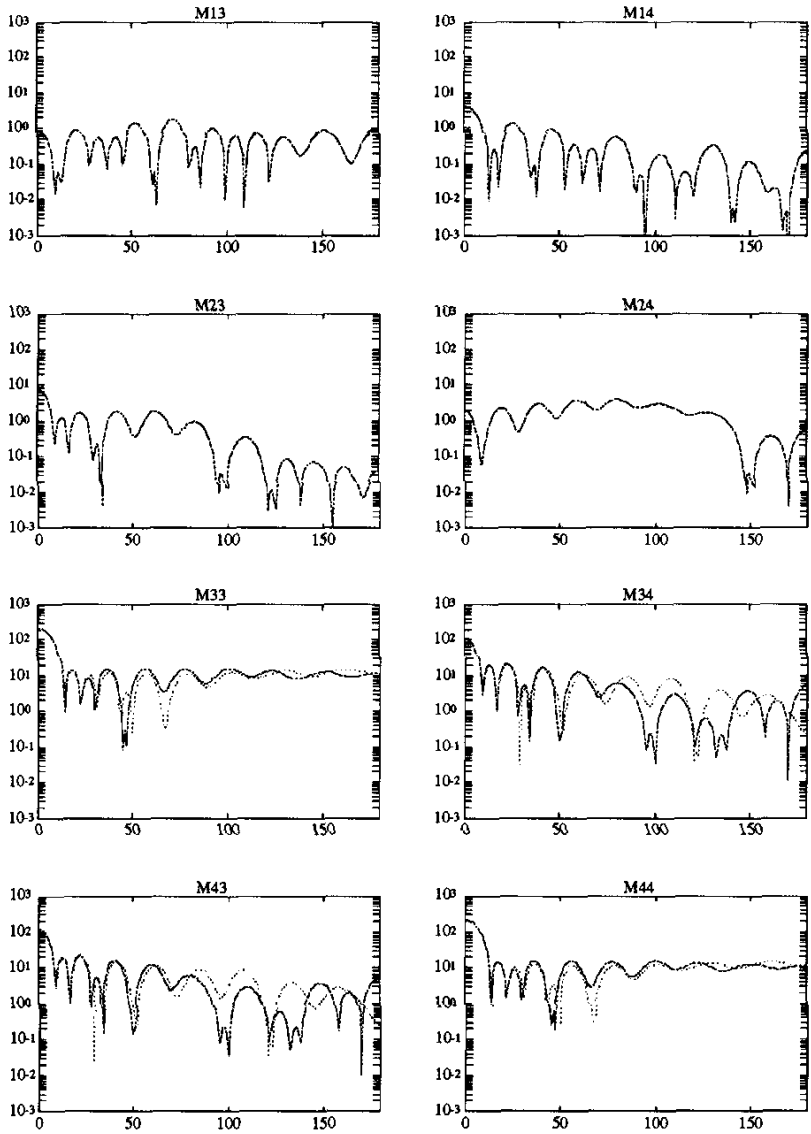

Figure 5. Elements of the Mueller scattering matrix plotted for the coated conducting cylinder as a function of scattering angle (dotted line = achiral case, solid line = chiral case).

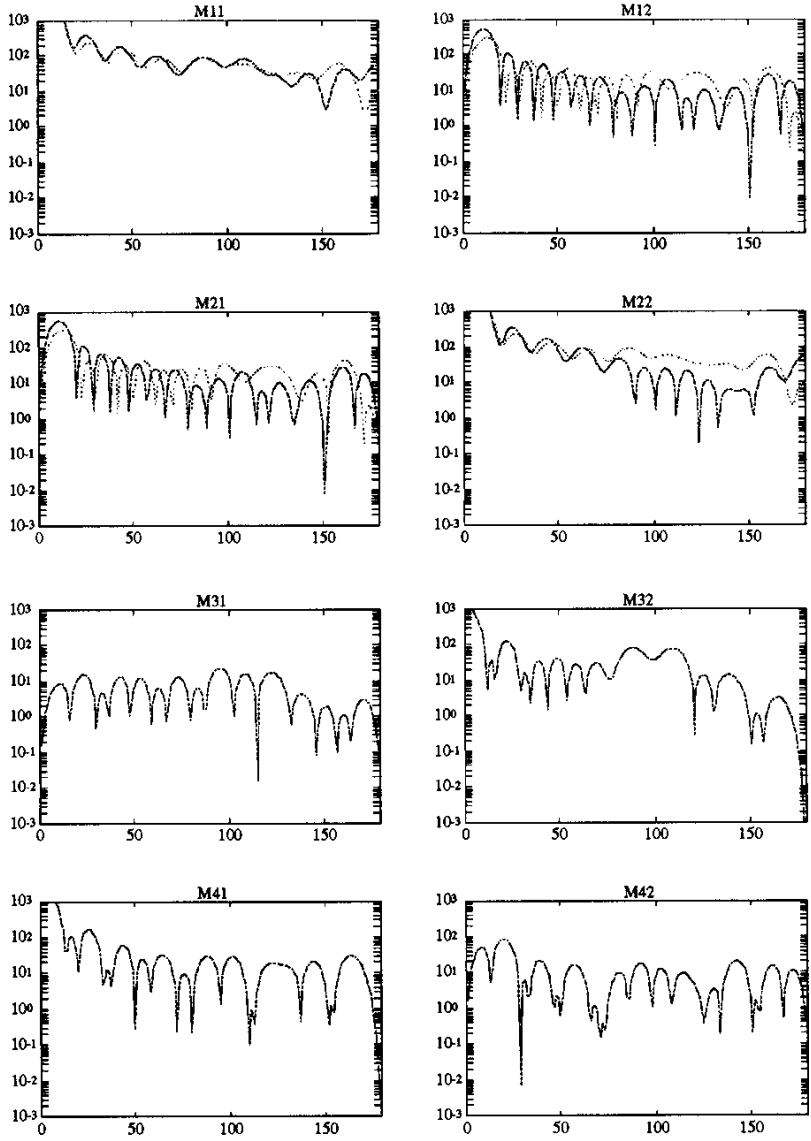

Figure 6. Elements of the Mueller scattering matrix plotted for the coated conducting sphere as a function of scattering angle (dotted line = achiral case, solid line = chiral case).

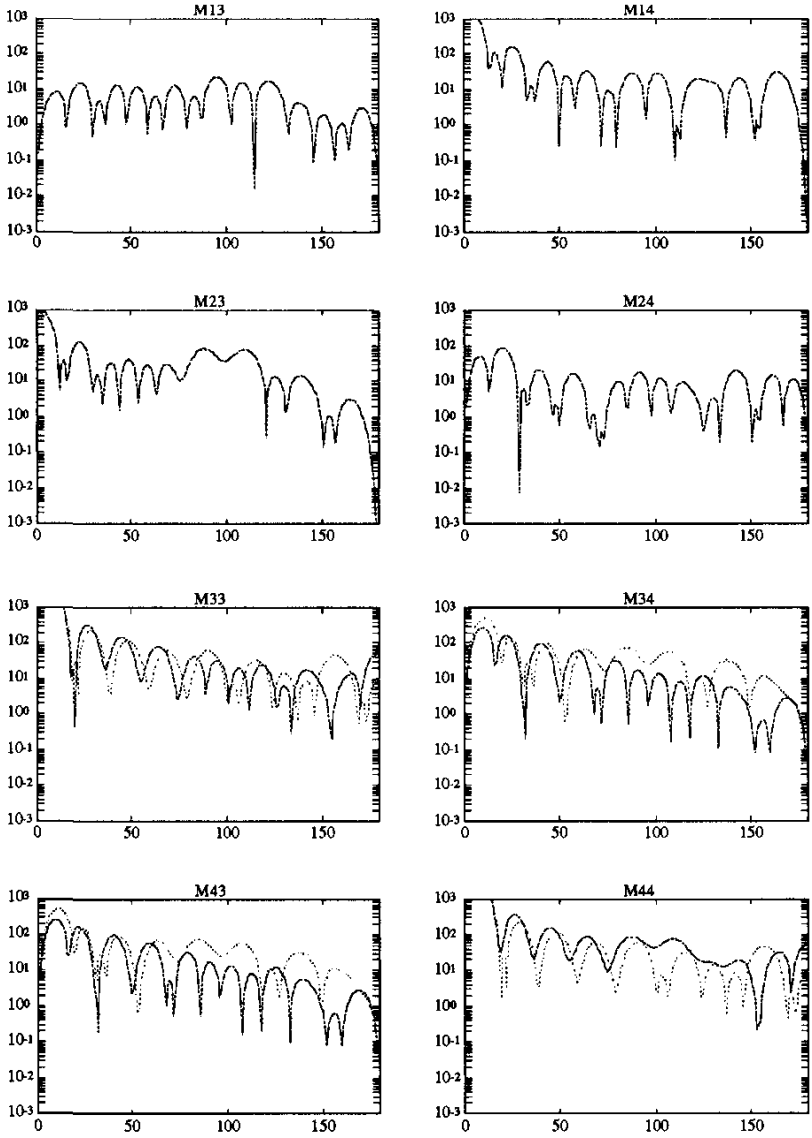

Figure 6. Elements of the Mueller scattering matrix plotted for the coated conducting sphere as a function of scattering angle (dotted line = achiral case, solid line = chiral case).

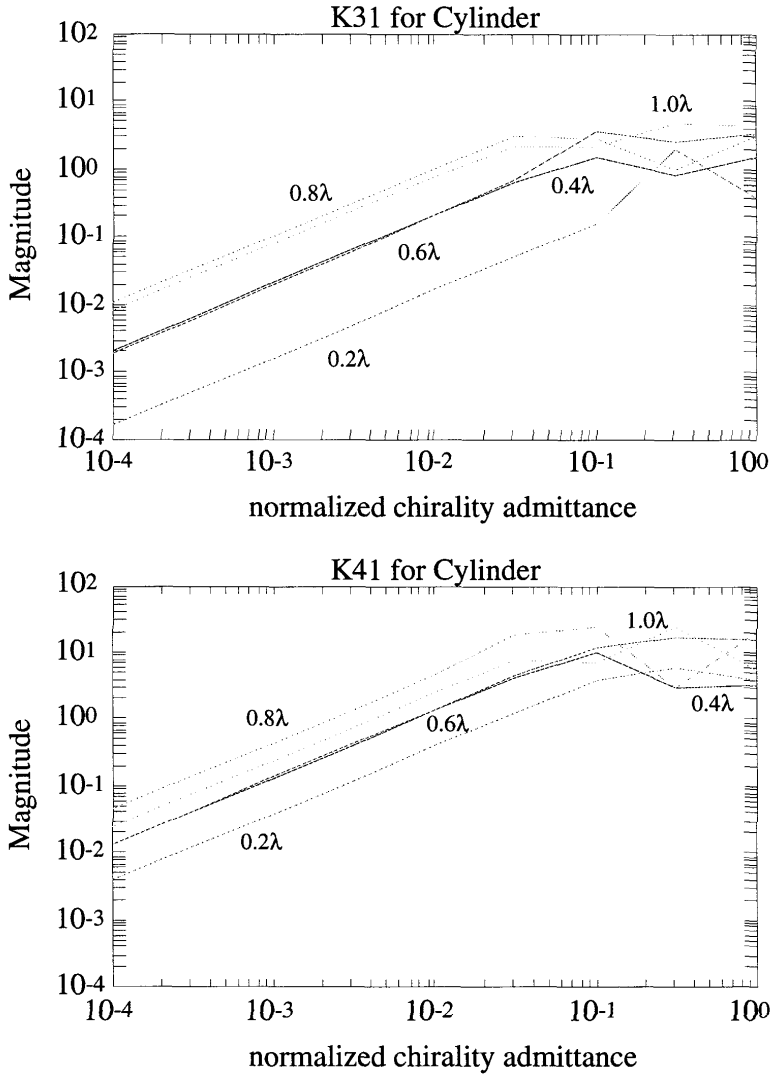

Figure 7. Relative power of the four most sensitive Mueller matrix elements plotted against chirality for the homogeneous chiral cylinder.

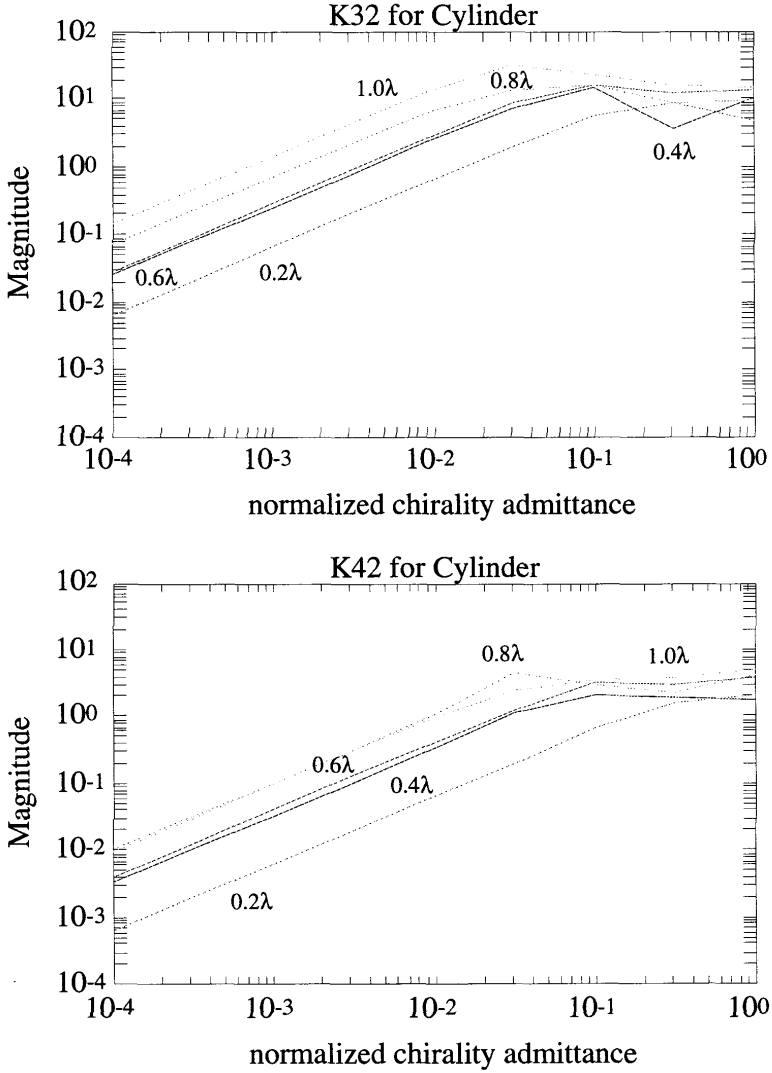

Figure 7. Relative power of the four most sensitive Mueller matrix elements plotted against chirality for the homogeneous chiral cylinder.

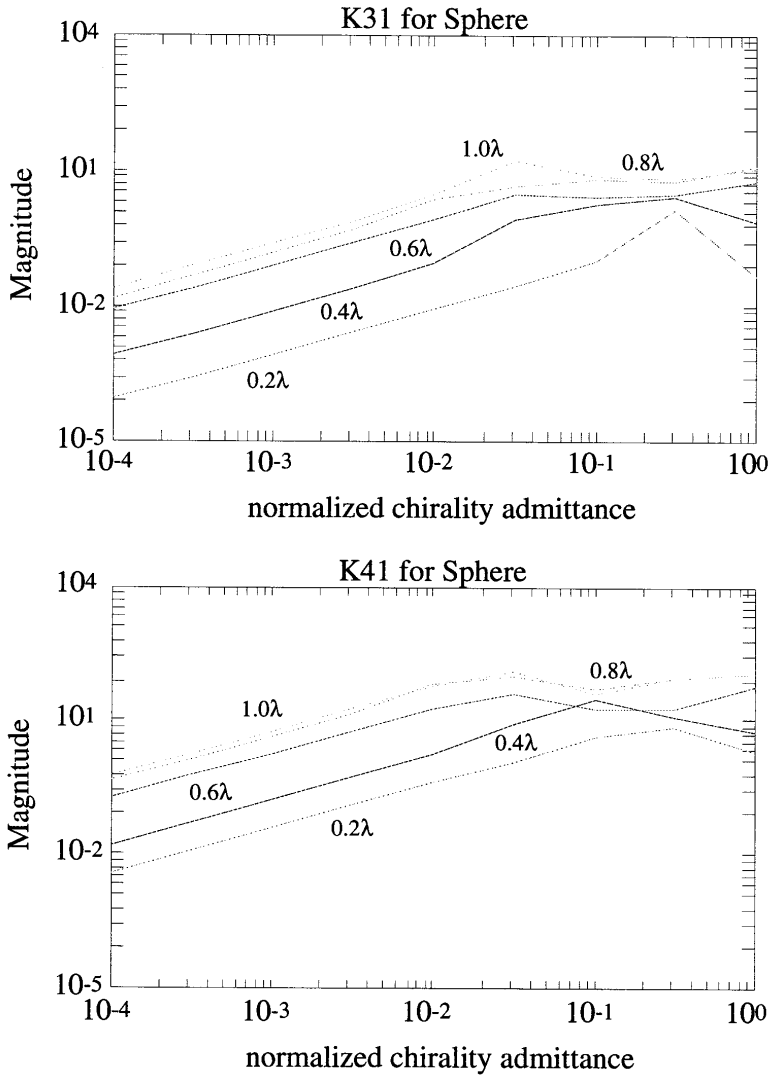

Figure 8. Relative power of the four most sensitive Mueller matrix elements plotted against chirality for the homogeneous chiral sphere.

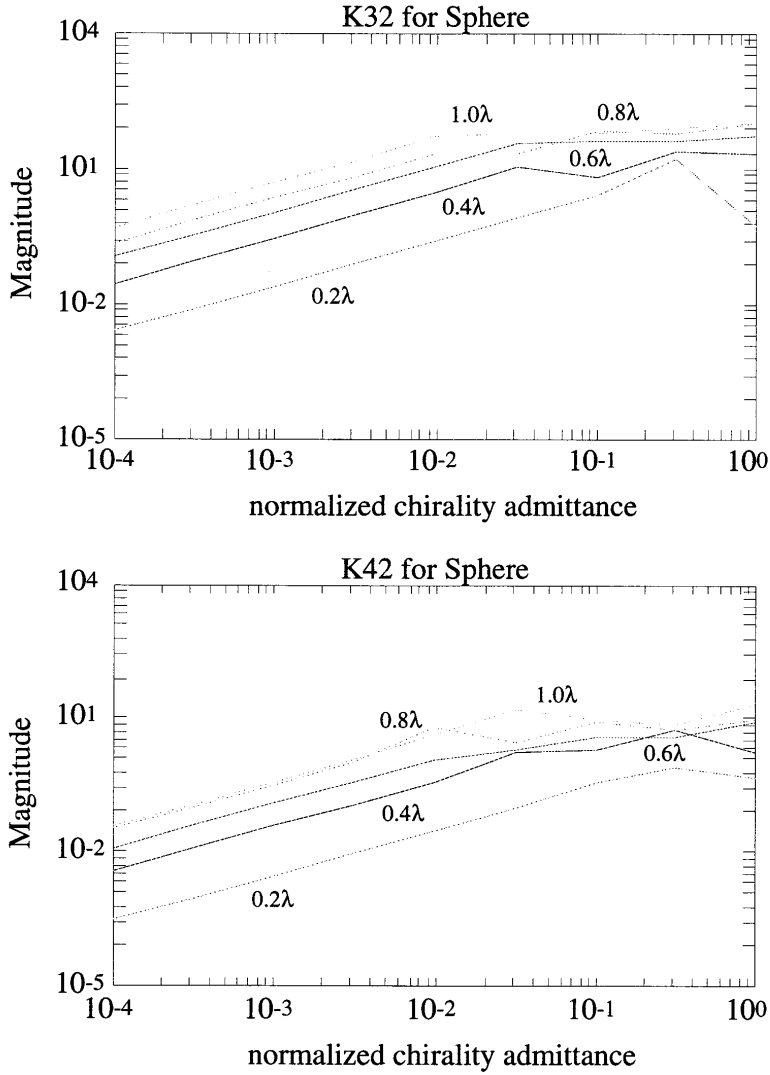

Figure 8. Relative power of the four most sensitive Mueller matrix elements plotted against chirality for the homogeneous chiral sphere.

and the results are plotted for varying material chirality. In the cases depicted in Figs. 7 and 8, the geometry is that of a homogeneous chiral cylinder and sphere, respectively, with radii of 0.2, 0.4, 0.6, 0.8 and 1.0 λ. For these cases, the metal core has been removed to isolate and emphasize the effects of chirality. In general, the larger the diameter, the greater the effect of chirality and the larger the magnitude in the plots. For smaller values of chirality, the log power in these Mueller matrix elements approximately vary in a linearly manner with the log of chirality. This linear relation for small values of chirality is consistent with perturbation theory. For larger values, the power in these elements tends to saturate, since the total intensity scattered is limited by the incident intensity. It is noted that for even very small chirality, the power in these Mueller matrix elements is significant. This suggests that with knowledge of the electromagnetic size of a material, the degree of chirality of the material can be remotely determined through observation of the K_{31}, K_{32}, K_{41}, and K_{42} parameters given in (40)–(41).

4. Conclusion

Here, we examine in detail the angular scattering from chiral-coated and homogeneous chiral objects using Mueller matrices. The addition of chirality introduces circular birefringence, that is, incident waves of different handedness "see" scatterers of different electromagnetic size. This is evident from the splitting and shifting of nulls of the co-polar scattering cross-section levels in both the cylindrical and spherical geometries. Waves of one handedness see a smaller cylinder or sphere than waves of the opposite handedness which is expected due to the difference in wavenumbers of each wave. As a result, the nulls of the scattering patterns characteristic of size are shifted in accordance with their polarization.

Chirality also alters the impedance of the chiral coating which changes the magnitude of the cross- and co-polar scattering strengths due to Fresnel-like reflections and interference. These effects are distinct from the depolarization effect of geometry. The latter are exhibited in the co-polar backscatter and cross-polar forward scattering cross-sections. These cross-sections are zero for the spherical case and non-zero for the cylindrical case. Of particular practical interest,

we note that the cross-polar backscattering results can be predicted from an extension of planar results for curved objects of modest size or larger, that is, for the case where the scatterer radius is equal or greater than one wavelength.

When chirality is present, the Mueller matrix elements M_{31}, M_{32}, M_{41}, and M_{42} are non-zero with average values that are simple functions of the degree of chirality for a wide range of values. The presence of these matrix elements with finite values is in counterdistinction to the achiral cases usually examined. Furthermore, these results are observable for small or modest sized cylinders and spheres and for very thin coatings. This suggests that the existence and degree of chirality of a material can be determined through remote observation of these Mueller matrix elements. These elements are highly sensitive to the degree of chirality and are significant for very small values of chirality and so become prime candidates for the remote detection and characterization of chirality in scatterers. In addition they are a demonstration of the symmetry properties of Mueller matrices first examined by Perrin. For all of these reasons, the result of finite Mueller matrix elements M_{31}, M_{32}, M_{41}, and M_{42} lead us to believe that further research in this area of electromagnetic chirality will be fruitful.

Appendix

Cylindrical Scattering Coefficients

The $\mathbf{A}_n$ and $\mathbf{B}_n$ incident wave cases will be considered separately. Consider an incident wave of the form,

$$\left\{ \begin{array}{c} \mathbf{E}_i \\ i\eta_0 \mathbf{H}_i \end{array} \right\} = \sum_{n=-\infty}^{\infty} \mathbf{A}_n^{(1)}(k_0) \tag{A.1}$$

with η_0 and k_0 equal to the free space impedance and wavenumber, respectively. Associated with this inward travelling cylindrical wave is a reflected wave,

$$\left\{ \begin{array}{c} \mathbf{E}_r \\ i\eta_0 \mathbf{H}_r \end{array} \right\} = \sum_{n=-\infty}^{\infty} \mathbf{r}_n^{aa} \mathbf{A}_n^{(3)}(k_0) \pm \mathbf{r}_n^{ab} \mathbf{B}_n^{(3)}(k_0) \tag{A.2}$$

The wave within the layer is given by,

$$\left\{ \begin{array}{c} \mathbf{E}_c \\ i\eta_c \mathbf{H}_c \end{array} \right\} = \sum_{n=-\infty}^{\infty} a_n \mathbf{A}_n^{(1)}(k_+) \pm b_n \mathbf{B}_n^{(1)}(k_-) + c_n \mathbf{A}_n^{(3)}(k_+) \pm d_n \mathbf{B}_n^{(3)}(k_-). \tag{A.3}$$

Applying boundary conditions at the inner and outer surfaces of the chiral layer, one can solve the resulting set of simultaneous equations to determine the scattering coefficients $\mathbf{r}_n^{aa}$ and $\mathbf{r}_n^{ab}$. In a similar fashion, the scattering coefficients $\mathbf{r}_n^{ba}$ and $\mathbf{r}_n^{bb}$ can be found by assuming an incident wave of the form $\mathbf{B}_n^{(1)}(k_0)$.

Matching boundary conditions, we find the scattering coefficients by solving the matrix,

$$\begin{bmatrix} B_0 & B_0 & -A_+ & -A_- & -B_+ & -B_- \\ D_0 & -D_0 & -C_+ & C_- & -D_+ & D_- \\ B_0 & -B_0 & -\gamma A_+ & \gamma A_- & -\gamma B_+ & \gamma B_- \\ D_0 & D_0 & -\gamma C_+ & -\gamma C_- & -\gamma D_+ & -\gamma D_- \\ 0 & 0 & E_+ & E_- & F_+ & F_- \\ 0 & 0 & G_+ & -G_- & H_+ & -H_- \end{bmatrix} \begin{bmatrix} \mathbf{r}_n^{aa} \\ \mathbf{r}_n^{ab} \\ a_n \\ b_n \\ c_n \\ d_n \end{bmatrix} = \begin{bmatrix} A_0 \\ C_0 \\ -A_0 \\ -C_0 \\ 0 \\ 0 \end{bmatrix} \tag{A.4}$$

where,

$$\begin{aligned} A_0 &= k_0 J_n'(k_0 b) & B_0 &= k_0 H_n^{(1)'}(k_0 b) \\ C_0 &= k_0 J_n(k_0 b) & D_0 &= k_0 H_n^{(1)}(k_0 b) \\ A_\pm &= k_\pm J_n'(k_\pm b) & B_\pm &= k_\pm H_n^{(1)'}(k_\pm b) \\ C_\pm &= k_\pm J_n(k_\pm b) & D_\pm &= k_\pm H_n^{(1)}(k_\pm b) \\ E_\pm &= k_\pm J_n'(k_\pm a) & F_\pm &= k_\pm H_n^{(1)'}(k_\pm a) \\ G_\pm &= k_\pm J_n(k_\pm a) & H_\pm &= k_\pm H_n^{(1)}(k_\pm a). \end{aligned} \tag{A.5}$$

Here, $\gamma = \eta_0/\eta_c$ is equal to the ratio of the free space impedance to the chiral impedance of the chiral coating.

Spherical Scattering Coefficients

To determine the scattering of the coated sphere configuration, the incident wave is considered of the form,

$$\left\{ \begin{array}{c} \mathbf{E}_i \\ i\eta_0 \mathbf{H}_i \end{array} \right\} = \sum_{n=1}^{\infty} \mathbf{A}^{(1)}_{\substack{e \\ 0} mn}(k_0) \tag{A.6}$$

and a reflected wave,

$$\left\{ \begin{array}{c} \mathbf{E}_r \\ i\eta_0 \mathbf{H}_r \end{array} \right\} = \sum_{n=1}^{\infty} \Gamma^{aa}_{mn} \mathbf{A}^{(3)}_{\substack{e \\ 0} mn}(k_0) \pm \Gamma^{ab}_{mn} \mathbf{B}^{(3)}_{\substack{e \\ 0} mn}(k_0). \tag{A.7}$$

The wave within the chiral layer is given by,

$$\begin{aligned} \left\{ \begin{array}{c} \mathbf{E}_c \\ i\eta_c \mathbf{H}_c \end{array} \right\} = & \sum_{n=1}^{\infty} a_{mn} \mathbf{A}^{(1)}_{\substack{e \\ 0} mn}(k_+) \pm b_{mn} \mathbf{B}^{(1)}_{\substack{e \\ 0} mn}(k_-) + \\ & c_{mn} \mathbf{A}^{(3)}_{\substack{e \\ 0} mn}(k_+) \pm d_{mn} \mathbf{B}^{(3)}_{\substack{e \\ 0} mn}(k_-). \end{aligned} \tag{A.8}$$

As with the cylindrical case, applying boundary conditions at the inner and outer surfaces of the chiral layer leads to a set of simultaneous equations which can be solved to yield the scattering coefficients Γ^{aa}_{mn} and Γ^{ab}_{mn}. The scattering coefficients Γ^{ba}_{mn} and Γ^{bb}_{mn} can be similarly determined by assuming an incident wave of the form $\mathbf{B}^{(1)}_{\substack{e \\ 0} mn}(k_0)$.

We find the scattering coefficients by solving the matrix,

$$\begin{bmatrix} x^v \\ y^v \\ x^v \\ y^v \\ 0 \\ 0 \end{bmatrix} = \begin{bmatrix} t_{11} & t_{12} & t_{13} & t_{14} & t_{15} & t_{16} \\ t_{21} & t_{22} & t_{23} & t_{24} & t_{25} & t_{26} \\ t_{11} & -t_{12} & \gamma t_{13} & \gamma t_{14} & -\gamma t_{15} & -\gamma t_{16} \\ t_{21} & -t_{22} & \gamma t_{23} & \gamma t_{24} & -\gamma t_{25} & -\gamma t_{26} \\ 0 & 0 & t_{53} & t_{54} & t_{55} & t_{56} \\ 0 & 0 & t_{63} & t_{64} & t_{65} & t_{66} \end{bmatrix} \begin{bmatrix} \Gamma^{aa}_{\substack{e \\ 0} mn} \\ \Gamma^{ab}_{\substack{e \\ 0} mn} \\ a_{mn} \\ b_{mn} \\ c_{mn} \\ d_{mn} \end{bmatrix} \tag{A.9}$$

where $\gamma = \eta_0/\eta_c$ and,

$$
\begin{array}{lll}
j_{\pm} = j_n(k_{\pm}r) & \text{and} & \partial j_{\pm} = \frac{1}{k_{\pm}r}\frac{\partial}{\partial r}\left[r j_n(k_{\pm}r)\right] \\
h_{\pm} = h_n^{(1)}(k_{\pm}r) & \text{and} & \partial h_{\pm} = \frac{1}{k_{\pm}r}\frac{\partial}{\partial r}\left[r h_n^{(1)}(k_{\pm}r)\right] \\
P = \frac{P_n^m(\cos\theta)}{\sin\theta} & \text{and} & \partial P = \frac{\partial P_n^m(\cos\theta)}{\partial\theta} \\
C = \left\{\begin{smallmatrix}\cos\\ \sin\end{smallmatrix}\right\}(m\phi) & \text{and} & S = \left\{\begin{smallmatrix}\sin\\ \cos\end{smallmatrix}\right\}(m\phi) \\
j = j_n(k_0 r) & \text{and} & \partial j = \frac{1}{k_0 r}\frac{\partial}{\partial r}\left[r j_n(k_0 r)\right] \\
h = h_n^{(1)}(k_0 r) & \text{and} & \partial h = \frac{1}{k_0 r}\frac{\partial}{\partial r}\left[r h_n^{(1)}(k_0 r)\right]
\end{array}
\tag{A.10}
$$

and with,

$$
\begin{aligned}
x^v &= \mp(mjPS) + (\partial j \partial PC)|_{r=b} \\
&\quad \text{and} \quad y^v = -(j\partial PC) \mp (m\partial jPS)|_{r=b} \\
t_{11} &= \mp(mhPS) - (\partial h \partial PC)|_{r=b} \\
&\quad \text{and} \quad t_{12} = \pm(mhPS) + (\partial h \partial PC)|_{r=b} \\
t_{13} &= \mp(mj_+PS) + (\partial j_+ \partial PC)|_{r=b} \\
&\quad \text{and} \quad t_{14} = \mp(mh_+PS) + (\partial h_+ \partial PC)|_{r=b} \\
t_{15} &= \mp(mj_-PS) - (\partial j_- \partial PC)|_{r=b} \\
&\quad \text{and} \quad t_{16} = \mp(mh_-PS) - (\partial h_- \partial PC)|_{r=b} \\
t_{21} &= (h\partial PC) \pm (m\partial hPS)|_{r=b} \\
&\quad \text{and} \quad t_{22} = (h\partial PC) \mp (m\partial hPS)|_{r=b} \\
t_{23} &= -(j_+\partial PC) \mp (m\partial j_+PS)|_{r=b} \\
&\quad \text{and} \quad t_{24} = -(h_+\partial PC) \mp (m\partial h_+PS)|_{r=b} \\
t_{25} &= -(j_-\partial PC) \pm (m\partial j_-PS)|_{r=b} \\
&\quad \text{and} \quad t_{26} = -(h_-\partial PC) \pm (m\partial h_-PS)|_{r=b} \\
t_{53} &= \mp(mj_+PS) + (\partial j_+ \partial PC)|_{r=a} \\
&\quad \text{and} \quad t_{54} = \mp(mh_+PS) + (\partial h_+ \partial PC)|_{r=a} \\
t_{55} &= \mp(mj_-PS) - (\partial j_- \partial PC)|_{r=a} \\
&\quad \text{and} \quad t_{56} = \mp(mh_-PS) - (\partial h_- \partial PC)|_{r=a}
\end{aligned}
$$

$$t_{63} = -(j_+ \partial PC) \mp (m \partial j_+ \partial PS)|_{r=a}$$
$$\text{and} \quad t_{64} = -(h_+ \partial PC) \mp (m \partial h_+ \partial PS)|_{r=a}$$
$$t_{65} = -(j_- \partial PC) \pm (m \partial j_- \partial PS)|_{r=a}$$
$$\text{and} \quad t_{66} = -(h_- \partial PC) \pm (m \partial h_- \partial PS)|_{r=a}. \tag{A.11}$$

Acknowledgment

This work was supported by a NATO Collabrative Research Grant No. 930923 and by the Complex Media Laboratory, University of Pennsylvania.

References

1. Jaggard, D. L., A. R. Michelson, and C. H. Papas, "On electromagnetic waves in chiral media," *Appl. Phys.,* Vol. 18, 211–216, 1979.
2. Jaggard, D. L., and N. Engheta, "Chirality in electrodynamics: modeling and applications," in *Directions in Electromagnetic Wave Modeling,* H. L. Bertoni and L. B. Felsen, editors, Plenum Publishing Co., New York, 435-446, 1991.
3. Bassiri, S., C. H. Papas, and N. Engheta, "Electromagnetic wave propagation through a dielectric-chiral interface and through a chiral slab," *J. Opt. Soc. Am. A,* Vol. 5, 1450–1459, 1988.
4. Jaggard, D. L., and N. Engheta, "Chirosorb^{TM} as an invisible medium," *Electron. Lett.,* Vol. 25, 173–174, 1989.
5. Jaggard, D. L., N. Engheta, and J. C. Liu, "Chiroshield^{TM}: a Salisbury/Dallenbach shield alternative," *Electron. Lett.,* Vol. 26, 1332–1333, 1990.
6. Oksanen, M. I., S. A. Tretyakov, and I. V. Lindell, "Vector circuit theory for isotropic and chiral slabs," *J. Electromag. Wave Appl.,* Vol. 4, 613–643, 1990.
7. Jaggard, D. L., and J. C. Liu, "Chiral layers on curved surfaces," *J. Electromag. Waves Appl.,* Vol. 5/6, 669–694, 1992.

8. Bohren, C. F., "Scattering of electromagnetic waves by an optically active cylinder," *J. Coll. Interface Sci.,* Vol. 66, 105–109, 1978.
9. Kluskens, M. S., and E. H. Newman, "Scattering by a multilayer chiral cylinder," *IEEE Trans. Ant. and Propagat.,* Vol. 39, 96–99, 1991.
10. Graglia, R. D., P. L. E. Uslenghi, and C. L. Yu, "Electromagnetic oblique scattering by a cylinder coated with chiral layers and anisotropic jump-immitance sheets", *J. Electronmag. Waves Appl.,* Vol. 6, 695–720, 1992.
11. Bohren, C. F., "Light scattering by an optically active sphere," *Chem. Phys. Lett.,* Vol. 29, 458–462, 1974.
12. Bohren, C. F., "Scattering of electromagnetic waves by an optically active spherical shell," *J. Chem. Phys.,* Vol. 62, 1566–1571, 1975.
13. Lindell, I. V., and A. H. Sihvola, "Quasi-static analysis of scattering from a chiral sphere," *J. Electromag. Waves Appl.,* Vol. 4, 1223–1232, 1990.
14. Uslenghi, P. L. E., "Scattering by an impedance sphere coated with a chiral layer," *Electromagnetics,* Vol. 10, 201–211, 1990.
15. Lakhtakia, A., V. K. Varadan, and V. V. Varadan, "Scattering and absorption characteristics of lossy dielectric, chiral, nonspherial objects," *Appl. Opt.,* Vol. 24, 4146–4154, 1985.
16. Jaggard, D. L., J. C. Liu, A. Grot, and P. Pelet, "Thin wire scatterers in chiral media," *Optics Lett.,* Vol. 16, 781–783, 1991.
17. Jaggard, D. L., J. C. Liu, A. Grot, and P. Pelet, "Radiation and scattering from thin wires in chiral media," *IEEE Trans. Ant. and Propagat.,* Vol. 40, 1273–1282, 1992.
18. Stratton, J. A., *Electromagnetic Theory*, New York, McGraw-Hill, 1941.
19. Perrin, F., "Polarization of light scattered by isotropic opalescent media," *J. Chem. Phys.,* Vol. 10, 415–427, 1942.
20. Van de Hulst, H. C., *Light Scattering by Small Particles*, New York, Wiley, 1957.